AGU ADVANCING EARTH AND SPACE SCIENCES

Earth and Space Science

RESEARCH ARTICLE
10.1029/2023EA003447

Evaluation of the Empirical Scaling Factor of Joule Heating Rates in TIE-GCM With EISCAT Measurements

Florian Günzkofer[1], Huixin Liu[2], Gunter Stober[3], Dimitry Pokhotelov[4], and Claudia Borries[1]

[1]Institute for Solar-Terrestrial Physics, German Aerospace Center (DLR), Neustrelitz, Germany, [2]Department of Earth and Planetary Sciences, Kyushu University, Fukuoka, Japan, [3]Institute of Applied Physics & Oeschger Center for Climate Change Research, Microwave Physics, University of Bern, Bern, Switzerland, [4]Institute of Physics, University of Greifswald, Greifswald, Germany

Key Points:

- The constant Joule heating scaling factor in TIE-GCM is inadequate to compensate for the underestimation under various geomagnetic conditions
- Joule heating rates calculated from 2,220 hr of EISCAT measurements are compared to TIE-GCM runs driven with the *Heelis* and *Weimer* convection models
- The required scaling factor varies significantly with the *Kp* index, the Kan-Lee merging electric field, and the magnetic local time

Correspondence to:

F. Günzkofer and H. Liu,
florian.guenzkofer@dlr.de;
liu.huixin.295@m.kyushu-u.ac.jp

Citation:

Günzkofer, F., Liu, H., Stober, G., Pokhotelov, D., & Borries, C. (2024). Evaluation of the empirical scaling factor of Joule heating rates in TIE-GCM with EISCAT measurements. *Earth and Space Science*, *11*, e2023EA003447. https://doi.org/10.1029/2023EA003447

Received 23 NOV 2023
Accepted 9 MAR 2024

Author Contributions:

Conceptualization: Florian Günzkofer, Huixin Liu
Formal analysis: Florian Günzkofer
Investigation: Florian Günzkofer
Methodology: Florian Günzkofer
Software: Florian Günzkofer
Supervision: Huixin Liu, Gunter Stober, Claudia Borries
Validation: Florian Günzkofer
Writing – original draft: Florian Günzkofer, Huixin Liu
Writing – review & editing: Huixin Liu, Gunter Stober, Dimitry Pokhotelov, Claudia Borries

Abstract

Joule heating is one of the main energy inputs into the thermosphere-ionosphere system. Precise modeling of this process is essential for any space weather application. Existing thermosphere-ionosphere models tend to underestimate the actual Joule heating rate quite significantly. The Thermosphere-Ionosphere-Electrodynamics General-Circulation-Model applies an empirical scaling factor of 1.5 for compensation. We calculate vertical profiles of Joule heating rates from approximately 2,220 hr of measurements with the EISCAT incoherent scatter radar and the corresponding model runs. We investigate model runs with the plasma convection driven by both the *Heelis* and the *Weimer* model. The required scaling of the Joule heating profiles is determined with respect to the *Kp* index, the Kan-Lee merging electric field E_{KL}, and the magnetic local time. Though the default scaling factor of 1.5 appears to be adequate on average, we find that the required scaling varies strongly with all three parameters ranging from 0.46 to ∼20 at geomagnetically disturbed and quiet times, respectively. Furthermore, the required scaling is significantly different in runs driven by the *Heelis* and *Weimer* model. Adjusting the scaling factor with respect to the *Kp* index, E_{KL}, the magnetic local time, and the choice of convection model would reduce the difference between Joule heating rates calculated from measurement and model plasma parameters.

Plain Language Summary

The vast majority of the energy input to the Earth system originates from the sun. This includes the absorption of various types of radiation, for example, ultraviolet radiation in the ozone layer or visible light and infrared radiation at the surface. In the upper atmosphere above about 80 km altitude, the absorption of extreme ultraviolet radiation and soft X-rays plays a major role. However, other processes also contribute significantly to the heating of this region, for example, the energy dissipation in the form of electric currents flowing along electric fields, also known as Joule heating. Joule heating is highly variable and can be drastically enhanced especially during solar storms, which can have potentially disastrous effects on satellites. Accurate modeling, and therefore also prediction, of Joule heating is not possible at the moment since thermosphere-ionosphere models have to scale the Joule heating empirically to fit the actual values. We investigate how the required scaling changes under different geophysical conditions.

1. Introduction

Heating in the upper atmosphere is caused by several different mechanisms and their respective impacts vary strongly with geomagnetic activity and location. Ionospheric modeling and space weather prediction require understanding and accurately describing these processes such as energetic particle precipitation or absorption of extreme ultraviolet and soft X-ray radiation. At high latitudes, especially during geomagnetic active periods, the *Joule heating* due to the dissipation of ionospheric currents is of major importance for the ionosphere-thermosphere system. The local Joule heating rate is defined as

$$q_J = \mathbf{j} \cdot (\mathbf{E} + \mathbf{u} \times \mathbf{B}) \tag{1}$$

with the current density $\mathbf{j}$, the electric field $\mathbf{E}$, the neutral wind $\mathbf{u}$, and the magnetic field $\mathbf{B}$.

At high latitudes, ionospheric currents are associated with the polar plasma convection, which results from the interaction of the Earth's magnetic field and the interplanetary magnetic field (IMF) carried by the solar wind (e.g., Baumjohann & Treumann, 1996; Kelley, 2009; Schunk & Nagy, 2009). The convection pattern gives rise to an electric field $\mathbf{E}_\perp$ perpendicular to the nearly vertical magnetic field lines. In this situation, two types of currents

can be distinguished: Pedersen currents $\mathbf{j}_P(\|\mathbf{E}_\perp)$ parallel to the electric field and Hall currents $\mathbf{j}_H(\|\mathbf{E}_\perp \times \mathbf{B})$ perpendicular to both the electric field and the magnetic field lines. From Equation 1, it can be seen that only Pedersen currents contribute to the Joule heating rate. Introducing the Pedersen conductivity σ_P, the Pedersen current can be written as $\mathbf{j}_P = \sigma_P(\mathbf{E}_\perp + \mathbf{u} \times \mathbf{B})$. Including the neutral dynamo effect due to the neutral wind $\mathbf{u}(z)$, the altitude-dependent Joule heating rate is

$$q_J(z) = \sigma_P(z)(\mathbf{E}_\perp + \mathbf{u}(z) \times \mathbf{B}(z))^2 \quad \left[\mathrm{Wm}^{-3}\right]. \tag{2}$$

Integration of Equation 2 gives the height-integrated Joule heating rate

$$Q_J = \int_{z_1}^{z_2} \sigma_P(z)(\mathbf{E}_\perp + \mathbf{u}(z) \times \mathbf{B}(z))^2 \mathrm{d}z \quad \left[\mathrm{Wm}^{-2}\right]. \tag{3}$$

Assuming empirical neutral atmosphere densities and winds, the height-integrated Joule heating rate Q_J can be determined from satellite observations (e.g., Foster et al., 1983; Palmroth et al., 2005; Rich et al., 1991). To determine the vertical profile of the local Joule heating rate q_J, incoherent scatter radar (ISR) measurements can be applied (e.g., Kavanagh et al., 2022; Thayer, 1998, 2000; Vickrey et al., 1982). Global thermosphere-ionosphere (T-I) models provide vertical profiles of q_J at all geographic locations and are therefore a valuable addition to local ISR measurements (e.g., Deng & Ridley, 2007; Deng et al., 2009; Huang et al., 2012; Maute, 2017; Weimer, 2005). However, it has been noted that T-I models tend to underestimate the actual Joule heating rate quite significantly (Codrescu et al., 1995; Deng & Ridley, 2007). The Thermosphere-Ionosphere-Electrodynamics Global-Circulation-Model (TIE-GCM) (Richmond et al., 1992) therefore multiplies the Joule heating rate by a constant empirical factor of $f = 1.5$ (Codrescu et al., 1995; Emery et al., 1999). This study aims to investigate the required scaling factor under various conditions and whether a constant $f = 1.5$ is actually appropriate. For this purpose, we will compare TIE-GCM Joule heating rates (q_J^M and Q_J^M) with Joule heating rates that are calculated from TIE-GCM neutral parameters and EISCAT ISR plasma parameters measurements, that is, electric field and electron density, (q_J^E and Q_J^E).

An important point to consider is the representation of the polar plasma convection in T-I models. Since the plasma convection depends on the interaction of the IMF with the Earth's magnetic field, a physical convection model would require coupled modeling of the solar wind, the magnetosphere, and the ionosphere. However, ionosphere-thermosphere models generally apply empirical convection models. Two of the most commonly applied convection models are the *Heelis* model (Heelis et al., 1982) and the *Weimer* model (Weimer, 2005). The *Heelis* model applies the *Kp* index as an input parameter which quantifies the geomagnetic activity from global magnetometer measurements. The *Weimer* model fits the electrostatic potential for given solar wind/IMF parameters using a set of spherical harmonics (Weimer, 2005). We use the Kan-Lee merging electric field E_{KL} (Kan & Lee, 1979) to combine the solar wind and IMF parameters applied by the *Weimer* convection model. It has been found that E_{KL} correlates well with the polar cap potential (Weimer, 1995). The Kan-Lee merging electric field is defined as

$$E_{KL} = v_{sw} B_T \sin^2\left(\frac{\theta}{2}\right) \tag{4}$$

with the solar wind velocity v_{sw}, $B_T = \left(B_y^2 + B_z^2\right)^{0.5}$, and $\theta = \arctan\left(B_y / B_z\right)$, with the interplanetary magnetic field components B_y and B_z in the GSM coordinate system (Laundal & Richmond, 2017). Since the TIE-GCM can be driven by both the *Heelis* and the *Weimer* convection models, we will compare the performance of both models within TIE-GCM to obtain Joule heating rates for different forcing conditions. It has been shown that the Joule heating rate strongly depends on the magnetic local time (MagLT) (Baloukidis et al., 2023; Foster et al., 1983) and therefore we will also investigate how the required f factor varies with MagLT.

Section 2 will introduce the EISCAT ISR instrument and the TIE-GCM. The applied measurement mode as well as the geophysical conditions during the measurements will be described. In Section 3, we will show how local and height-integrated Joule heating rates are calculated from both measurements and model results. This includes an introduction to the *stochastic inversion* method that is applied to obtain 3D ion velocity and electric field

Table 1
Distribution of Measurement Time With the Kp Index and E_{KL}

Kp	Measurement time (hr)	E_{KL} (mVm^{-1})	Measurement time (hr)
0	186.6	**0–0.1**	484.2
0.333	311	**0.1–0.2**	328.2
0.667	263.5	**0.2–0.35**	410.8
1	195.7	**0.35–0.5**	360.9
1.333	160.3	**0.5–0.7**	245.1
1.667	182.5	**0.7–0.9**	130.9
2	156.1	**0.9–1.15**	120.7
2.333–2.667	206.7	**1.15–1.6**	81.5
3–3.333	168	**>1.6**	60.5
3.667–4	125		
4.333–5	139		
5.333–6	62.1		
>6	35.6		
∑	**2,192.1**	∑	**2,222.8**

vectors from ISR measurements. The comparison of Joule heating rates calculated completely from model results q_J^M and constrained with EISCAT measurements q_J^E is shown in Section 4. The evaluation of the empirical Joule heating scaling factor is presented in Section 4 as well and Section 5 discusses the obtained results. Section 6 will conclude the paper and give an outlook on possible future investigations.

2. Measurements and Models

2.1. EISCAT UHF Incoherent Scatter Radar

The EISCAT Ultra High Frequency (UHF) ISR at Tromsø, Norway (69.6°N, 19.2°E) (Folkestad et al., 1983) has a peak transmission power of about 1.5–2 MW. The radar transmission frequency is 930 MHz and the employed dish has a diameter of 32 m. This results in a beam width of about 0.7° corresponding to an antenna directive gain of approximately 48.1 dBi.

To obtain 3D electric field vectors, the EISCAT ISR can either be operated in combination with two remote receivers (tristatic) or in a beam-swing mode (monostatic) (Kavanagh et al., 2022). For this study, we will analyze approximately 2,220 hr of EISCAT measurements in the beam-swing mode, also known as *Common Program (CP)* 2. In this mode, the radar dish is rotated through four measurement positions with a total cycle time of 6 min, and the beam-aligned ion velocity is measured in each position. The time resolution of ∼0.1 hr results in approximately 22,200 measurement points. The EISCAT *CP* 2 and other experiment modes are described in Tjulin (2021).

Table 2
Distribution of Measurement Time in Hours With Respect to the Kp Index and MagLT

Kp/MagLT	03–09	09–15	15–21	21–03	∑
0–2	312	380.7	406.7	356.3	**1,455.7**
2–4	128.3	136.7	137.4	97.3	**499.7**
4–9	51.3	45.2	66.5	73.7	**236.7**
∑	**491.6**	**562.6**	**610.6**	**527.3**	**2,192.1**

Following Nygrén et al. (2011), we perform a *stochastic inversion* to obtain the F-region 3D ion velocity vector. The ionospheric electric field can be calculated from the ion velocities. The method and its application in this study are described in more detail in Section 3. Other parameters available from the ISR measurements are the electron density N_e, and the ion/electron temperatures T_i and T_e. In the E-region, these parameters are binned in 13 altitude gates with a vertical resolution of 5 km at 95–125 and 10 km at 135–185 km altitude.

As mentioned before, we will investigate Joule heating rates for different geophysical conditions (*Kp* index and E_{KL}) and magnetic local times. Table 1 gives the distribution of measurement time with the *Kp* index and E_{KL}.

Table 3
Distribution of Measurement Time in Hours WIth Respect to E_{KL} and MagLT

E_{KL} (mVm^{-1})/MagLT	03–09	09–15	15–21	21–03	∑
0–0.2	164	213.5	215	219.9	**812.4**
0.2–0.5	183.5	225.4	181.1	181.7	**771.7**
>0.5	149	135.8	218.5	135.4	**638.7**
∑	**496.5**	**574.7**	**614.6**	**537**	**2,222.8**

Investigating the bins given in Table 1 is only possible if the values are taken throughout the entire day and MagLT variations are neglected. Tables 2 and 3 give the bin resolution and measurement time per bin if variations with the *Kp* index/E_{KL} and MagLT are investigated simultaneously.

A seasonal dependence of the Joule heating rate and the required scaling factor has been shown before (Emery et al., 1999; Foster et al., 1983). Figure 1 shows the distribution of the EISCAT measurements by day of year. It can be seen that most EISCAT CP2 measurements took place in January or around the September equinox. The distribution shown in Figure 1 does not allow to investigate the seasonal dependence of the Joule heating rates and the required scaling. For the results shown in this paper, all measurements have been considered independent of the day of year.

2.2. TIE-GCM

The Thermosphere-Ionosphere-Electrodynamic General-Circulation-Model (TIE-GCM) (Richmond et al., 1992) is a global model of the coupled ionosphere-thermosphere system. The lower boundary is at about 96 km altitude where atmospheric tides are specified by the Global Scale Wave Model (GSWM) (Hagan & Forbes, 2002, 2003). The TIE-GCM output is given on a 2.5° × 2.5° longitude-latitude grid. The vertical resolution is 1/4 in scale height units equivalent to a resolution of ∼2–18 km. The time resolution of the TIE-GCM is set to 30 s and the model output is given in 1 hr intervals. The solar activity is parameterized with the F10.7 solar flux which is measured daily. The range of F10.7 varies from ∼70–170 sfu (solar flux units). The database includes 2 days (09 and 13 September 2005) with exceptionally high solar flux conditions of F10.7 ∼ 700 sfu and F10.7 ∼ 300 sfu. The data presented in this paper was generated from several runs performed with the TIE-GCM Version 2.0.

As mentioned in Section 1, the polar plasma potential, and hence the electric field, is given by an empirical convection model. Both the *Heelis* model (Heelis et al., 1982) and the *Weimer* model (Weimer, 2005) can be applied for that purpose. We performed two TIE-GCM runs for each EISCAT measurement, driven with either of the two convection models. It should be mentioned explicitly that the model runs were performed using realistic F10.7 and *Kp* index and time-advanced solar wind/IMF parameters. The model data is binned into the same E-region altitude gates as the EISCAT plasma parameters. Since the model output intervals are larger than the

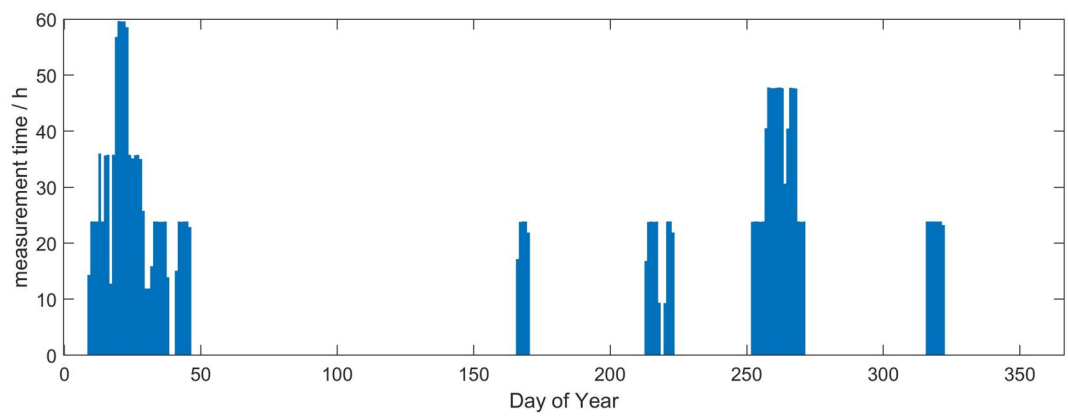

Figure 1. Seasonal distribution EISCAT measurement time included in the database.

measurement time resolution, we apply a nearest-neighbor interpolation on the model data. The same interpolation is performed on the *Kp* index and E_{KL} data. This allows to bin the Joule heating rates q_J^M and q_J^E according to Tables 1–3. Since there is a one-to-one correspondence of the *Kp* index and the solar wind/IMF parameters, it is valid to bin *Heelis*-driven runs with E_{KL} and *Weimer*-driven runs with the *Kp* index.

3. Method

The application of *stochastic inversion* to infer 3D ion velocity vectors from EISCAT beam-swing measurements is described in detail by Nygrén et al. (2011). We will summarize the implementation of the method for this paper and refer to Nygrén et al. (2011) for further information. The *stochastic inversion* method allows solving the linear problem

$$\mathbf{M} = \mathbf{A}\mathbf{x} + \epsilon \tag{5}$$

where the vector of unknown variables $\mathbf{x}$ is determined from the measurement vector $\mathbf{M}$ under consideration of the measurement uncertainties ϵ. This requires an adequate formulation of the theory matrix $\mathbf{A}$.

In the F-region ionosphere, the east- and northward ion velocities v_E^F and v_N^F can be assumed constant with altitude while the vertical ion velocity v_z^F changes with height (Nygrén et al., 2011). Therefore, the unknown vector $\mathbf{x}$ for each 6 min beam-swing cycle consists of one v_E^F value, one v_N^F values, and n_G $v_z^{F_G}$ values where n_G is the number of pre-defined F-region altitude gates. We define $n_G = 14$ altitude gates ranging from 230 to 515 km altitude with a resolution of 15 km (230–260 km), 20 km (280–360 km), and 25 km (390–515 km). Ideally, one measurement cycle consists of four pointing directions and therefore the total number of beam-aligned ion velocity measurements for each beam-swing cycle is $4 \cdot n_G$. Though F region electron densities are large enough to allow for ISR measurements at most times, it has to be considered that the fit of the incoherent scatter spectrum does not converge for one or more beams during some cycles. Beam-swing cycles with less than four converging ISR measurements are disregarded for the analysis in this paper. For each measurement position, the azimuth angle α and the elevation angle β are known and the measurements can be expressed by the standard radial wind equation

$$M_i^G = \sin\alpha_i \cos\beta_i v_E^F + \cos\alpha_i \cos\beta_i v_N^F + \sin\beta_i v_z^{F_G} \tag{6}$$

for $i = [1, 4]$. The transformation coefficients in Equation 6 give the ith line of the theory matrix $\mathbf{A}_G$ for a single altitude gate. Repeating this for each altitude gate gives the complete theory matrix $\mathbf{A}$ (see Nygrén et al., 2011, Equation 21).

Since the F-region ionosphere can be assumed to be collisionless, the perpendicular electric field can be approximated by the electric drift formula

$$\mathbf{E}_\perp = -\mathbf{v}^F \times \mathbf{B}. \tag{7}$$

As for the magnetic field B, the International Geomagnetic Reference Field (IGRF) (Alken et al., 2021; Barraclough, 1988) is employed. $\mathbf{E}_\perp$ is calculated at 300 km altitude and linearly scaled with the increasing magnetic field strength at lower altitudes, that is, the ratio of E-region to F-region magnetic field strength $B^E/B^F \approx 1.1$ (Nozawa et al., 2010). $\mathbf{E}_\perp$ can then be applied to calculate the local Joule heating rate in the E-region given by Equation 2. Numerical integration of the 13 E-region altitude gates gives the height-integrated Joule heating rate Q_J. Although the TIE-GCM gives the local Joule heating rate as an output variable, we calculate q_J^M from Equation 2 assuming the F-region $\mathbf{v}^F$ at 300 km altitude. This way, we ensure that any differences between q_J^M and q_J^E are due to the application of EISCAT plasma parameters and not due to any potential differences in the calculation method.

The Pedersen conductivity in Equation 2 is given as (Baumjohann & Treumann, 1996)

$$\sigma_P = \left(\frac{\nu_{en}}{\nu_{en}^2 + \Omega_e^2} + \frac{m_e}{m_i} \frac{\nu_{in}}{\nu_{in}^2 + \Omega_i^2} \right) \frac{N_e e^2}{m_e}. \tag{8}$$

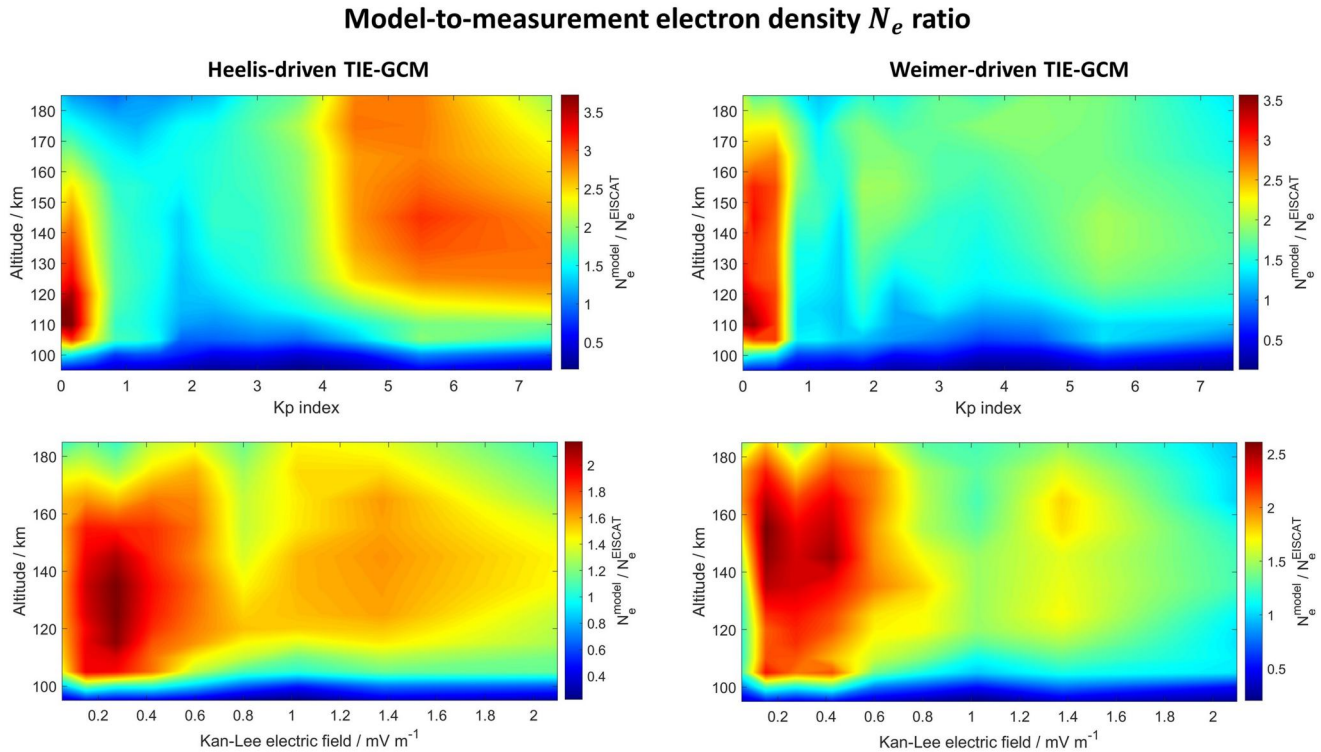

Figure 2. Ratio of electron densities N_e as given by TIE-GCM, driven with either *Heelis* or *Weimer* convection, to EISCAT measurements. The electron densities have been binned with respect to the *Kp* index and E_{KL}.

The ion/electron-neutral collision frequencies ν_{in} and ν_{en}, ion/electron gyro-frequencies Ω_i and Ω_e and the mean ion mass m_i are taken from TIE-GCM runs for the calculation of both q_J^M and q_J^E. The electron density N_e is taken from EISCAT measurements when calculating q_J^E and from the TIE-GCM output when calculating q_J^M. Whether the calculation of q_J^E should be done with model or measurement N_e, is up to discussion. Taking the model N_e would ensure that the differences of q_J^E and q_J^M are entirely caused by the plasma convection and therefore allow to evaluate the two convection models in comparison to ISR measurements. On the other hand, if the EISCAT ISR measured electron density is applied, q_J^E is closer to the actual Joule heating rate which is of interest when the empirical Joule heating scaling factor is adjusted. Therefore, the EISCAT measured N_e is applied for the calculation of q_J^E throughout the paper. Figure 2 gives the ratios of model-to-measurement electron density for both *Heelis*- and *Weimer*-driven runs binned with respect to the *Kp* index and E_{KL}. It can be seen from Equations 2 and 8 that this factor linearly propagates to the Joule heating rates.

The vertical profile of the neutral wind $\mathbf{u}(z)$ in Equations 2 and 3 is always taken from TIE-GCM. Especially for periods of low geomagnetic activity, the neutral wind contribution to the Joule heating rate can not be neglected (Baloukidis et al., 2023; Vickrey et al., 1982).

4. Results

After calculating q_J^M and q_J^E for each time-point, the profiles are binned with respect to the *Kp* index, E_{KL}, and MagLT. For each bin, a median profile $q_J^E(z)$ and two median profiles $q_J^M(z)$, one for *Heelis*- and one for *Weimer*-driven model runs, are calculated. The optimum empirical scaling factor f is determined by a non-linear least-square fit of $q_J^E(z) - f \cdot q_J^M(z) = 0$. This is demonstrated in Figure 3 for 230 hr of data during September 2005 with $Kp > 2$ conditions.

The model profiles in Figure 3a are linearly scaled to fit q_J^E which results in the profiles shown in Figure 3b. From the non-linear least-square fit, it is found that the optimum scaling factors for the model runs with *Heelis* and

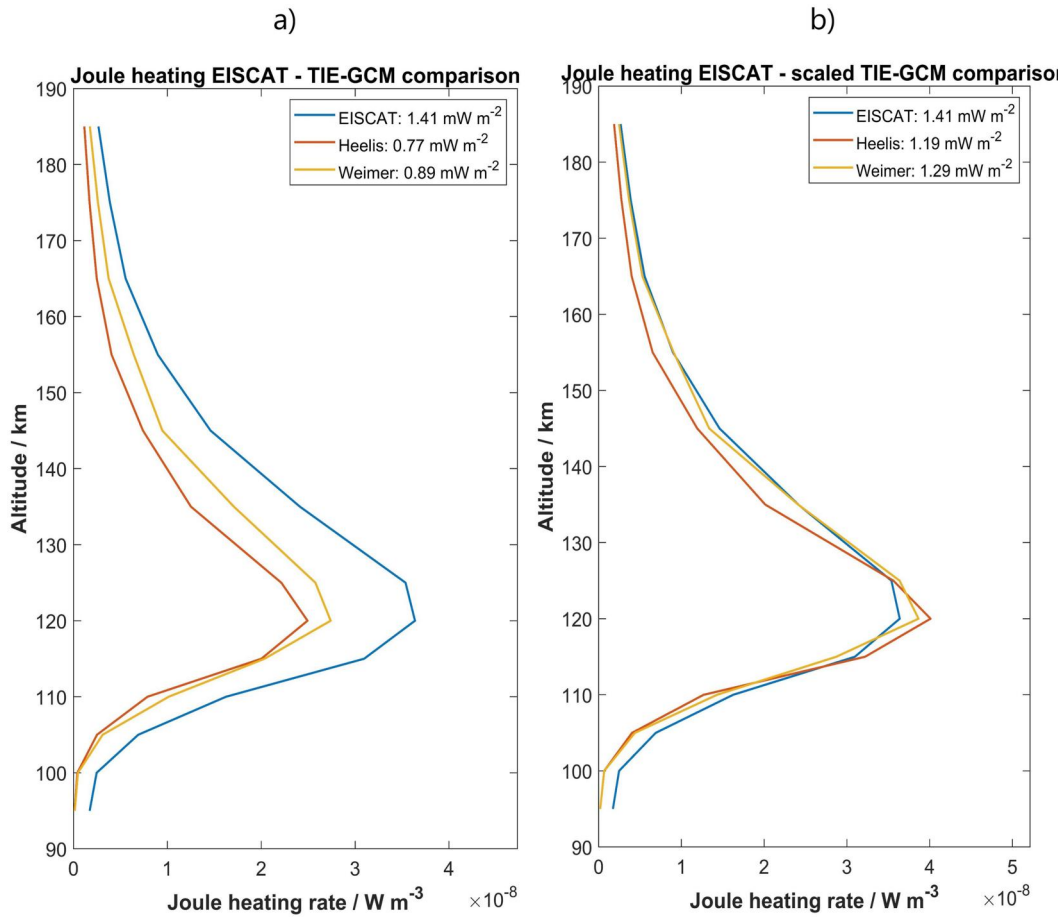

Figure 3. (a) Joule heating profiles q_J^E calculated with EISCAT plasma parameters and q_J^M calculated from TIE-GCM simulations with both *Heelis* and *Weimer* plasma convection for $Kp > 2$. (b) The two model profiles are scaled with the optimum scaling factors $f_H = 1.60$ and $f_W = 1.41$ to fit q_J^E.

Weimer plasma convection are $f_H = 1.60$ and $f_W = 1.41$. These are very close to the default value $f = 1.5$ in the TIE-GCM.

For further analysis, an extended database of approximately 2,220 hr of EISCAT measurements and TIE-GCM simulations is applied. The data is binned according to the Kp index and E_{KL} ranges given in Table 1. We investigate the optimum profile scaling factor f and the mean-squared difference of the vertical Joule heating rate profiles. The mean-squared difference is calculated as $MSD = 1/n_z \cdot \sum_{i=1}^{n_z} \left(q_{J,i}^E - q_{J,i}^M\right)^2$ where $n_z = 13$ is the number of altitude gates, and $q_{J,i}^E$ and $q_{J,i}^M$ are the discretized Joule heating rate profiles. We also investigate the absolute and relative difference between the height-integrated Joule heating rates Q_J^M and Q_J^E. Figure 4 shows the variation of these quantities with the Kp index.

For the TIE-GCM runs driven with the *Heelis* convection model, it can be seen in Figure 4a that the model would require a significantly larger scaling factor to fit the EISCAT-constrained Joule heating rates at $Kp < 4$ conditions. In Figures 4b–4d, the results are shown for the application of the default $f = 1.5$ and the optimized f from Figure 4a. An adjustment of the scaling factor reduces the MSD in Figure 4b by two orders of magnitude. Due to the generally lower Joule heating rates at $Kp < 4$, the absolute difference $\Delta Q_{abs} = Q_J^E - Q_J^M$ in Figure 4c is very low. Nevertheless, it can be seen that the height-integrated Joule heating rate gets slightly closer to Q_J^E by adjusting the scaling factor for *Heelis*-driven runs at $Kp < 4$. The relative difference $\Delta Q_{rel} = \left(Q_J^E - Q_J^M\right)/Q_J^E$ in Figure 4d would be notably reduced. For $Kp > 4$, the default scaling factor $f = 1.5$ seems to be appropriate or even too large for *Heelis*-driven TIE-GCM runs. The MSD of

10.1029/2023EA003447

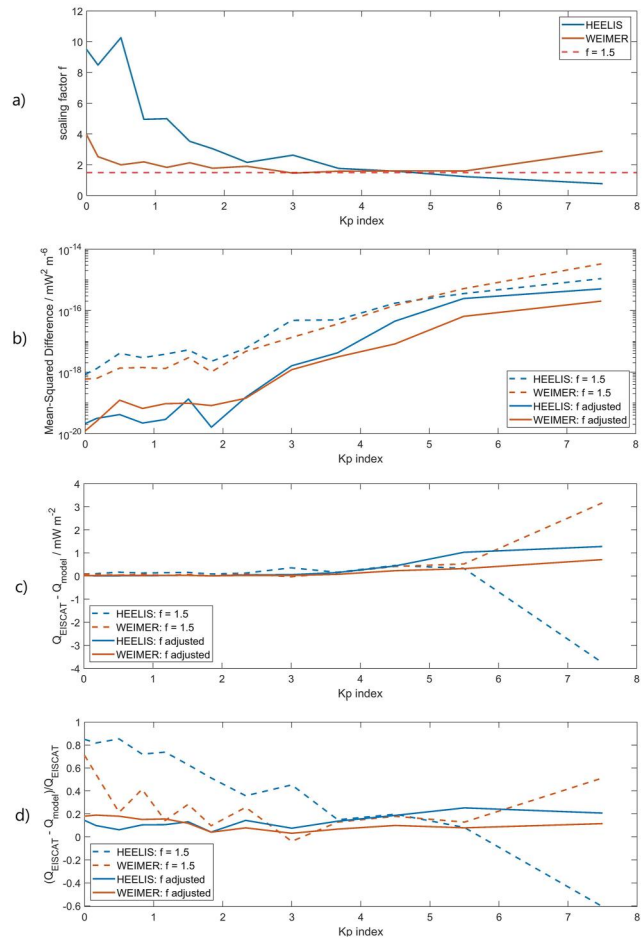

Figure 4. (a) Scaling factor f, (b) the mean-squared difference of q_J^M and q_J^E, (c) the absolute and (d) the relative difference of the height-integrated Joule heating rates Q_J^M and Q_J^E. The dotted lines in (b)–(d) give the results for $f = 1.5$ and the solid lines in case the scaling factors from (a) are applied to calculate the model Joule heating rate.

the Joule heating rate profiles is significantly larger at $Kp > 4$ than at lower geomagnetic activity and could be decreased by adjusting the scaling factor. However, ΔQ_{abs} and ΔQ_{rel} are actually increased for the adjusted scaling factor at $Kp \sim 5$. At $Kp > 5$, on the other hand, Q_J^M is far too high for the default $f = 1.5$ and adjusting the scaling factor would bring it significantly closer to Q_J^E.

The TIE-GCM runs driven with the *Weimer* convection model require a scaling factor $f > 1.5$ at $Kp < 4$ conditions. The *MSD* of q_J^M and q_J^E would be significantly reduced by adjusting the scaling factor. The relative difference would generally be reduced at $Kp < 4$ by adjusting the scaling factor while ΔQ_{abs} does not change notably. At $Kp > 5$, *Weimer*-driven model runs clearly underestimate the Joule heating rate. An adjustment of the scaling factor would significantly reduce the profile *MSD* as well as ΔQ_{abs} and ΔQ_{rel}.

In summary, the TIE-GCM results show very different behavior for *Heelis*- and *Weimer*-driven polar plasma convection. For the default scaling factor $f = 1.5$, the *Heelis*-driven model runs underestimate the Joule heating rate at $Kp < 4$ and overestimate it at $Kp > 5$. For *Weimer*-driven model runs, the default $f = 1.5$ seems to work considerably well at $Kp < 4$. While the *MSD* of the Joule heating rate profiles could be slightly decreased by adjusting the scaling factor, the height-integrated Joule heating rate would remain approximately the same. At $Kp > 4$, however, the Joule heating rates are clearly underestimated for the $f = 1.5$ case and an adjustment of the scaling factor would reduce the gap between the model Joule heating rates and those constrained by EISCAT measurements.

10.1029/2023EA003447

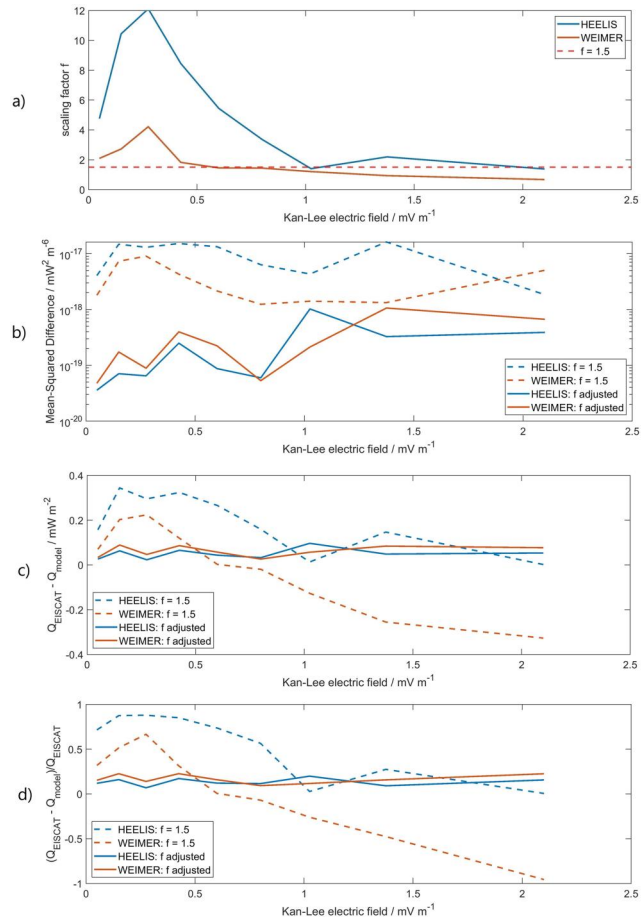

Figure 5. (a) Scaling factor f, (b) the mean-squared difference of q_J^M and q_J^E, (c) the absolute and (d) the relative difference of the height-integrated Joule heating rates Q_J^M and Q_J^E. The dotted lines in (b)–(d) give the results for $f = 1.5$ and the solid lines in case the scaling factors from (a) are applied to calculate the model Joule heating rate.

As mentioned in Section 1, the *Weimer* convection model determines the polar plasma potential from solar wind and IMF parameters. Therefore, the analysis above is repeated for the Kan-Lee merging electric field E_{KL} bins listed in Table 1. The results are shown in Figure 5.

The required scaling factor in Figure 5a shows that *Heelis*-driven TIE-GCM runs generally underestimate the Joule heating rate for most E_{KL} values. An adjustment of the scaling factor would reduce the *MSD* of the vertical Joule heating rate profiles by at least one order of magnitude for all E_{KL} values as shown in Figure 5b. This can also be seen in Figure 5c, where ΔQ_{abs} would be decreased by adjusting the scaling factor at all conditions with the exception of $E_{KL} \sim 1\ \mathrm{mVm}^{-1}$ and $E_{KL} \gtrsim 2\ \mathrm{mVm}^{-1}$. The same result is found for the relative difference in Figure 5d.

For the *Weimer*-driven model runs, it is found in Figure 5a that by applying a constant $f = 1.5$, the Joule heating rate is underestimated for $E_{KL} \lesssim 0.5\ \mathrm{mVm}^{-1}$ and overestimated for $E_{KL} \gtrsim 1\ \mathrm{mVm}^{-1}$. Figures 5c and 5d show that an adjustment of the scaling factor would reduce ΔQ_{abs} and ΔQ_{rel} for these E_{KL} ranges. Especially at $E_{KL} \gtrsim 1\ \mathrm{mVm}^{-1}$, the *Weimer*-driven model Joule heating rates would be significantly closer to the measurement-constrained results if the scaling factor is adjusted.

It has been reported previously that the Joule heating rate varies strongly with the magnetic local time (Baloukidis et al., 2023; Foster et al., 1983). We will therefore investigate the Joule heating rates separately for four MagLT bins covering the dawn sector (03–09 MagLT), the noon sector (09–15 MagLT), the dusk sector (15–21 MagLT), and the midnight sector (21–03 MagLT). To obtain enough measurement time in each investigated bin, the *Kp* index and E_{KL} bins are enlarged as stated in Tables 2 and 3. In total, we obtain vertical Joule heating rate profiles

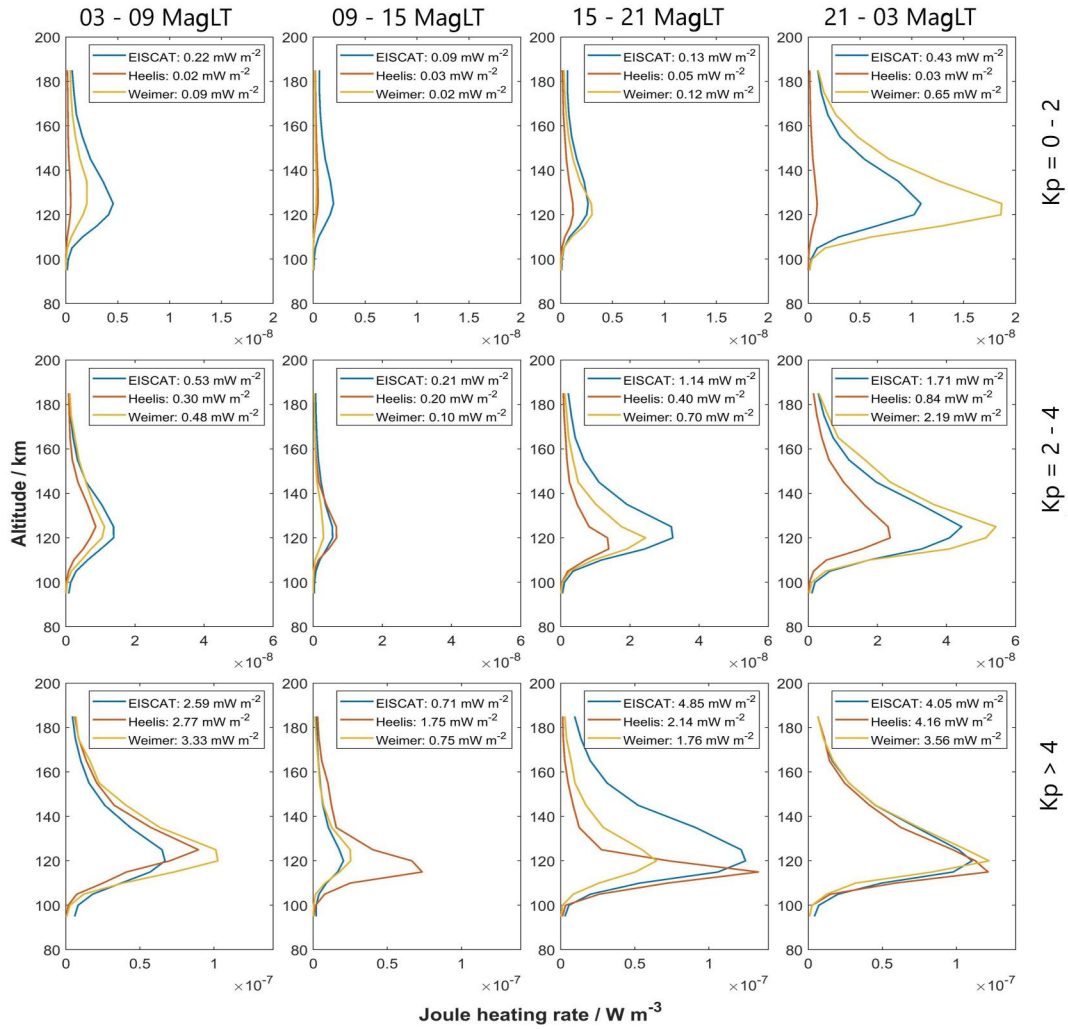

Figure 6. Median vertical profiles of the Joule heating rate q_J^M and q_J^E for 12 bins of varying *Kp* index and magnetic local time. The default $f = 1.5$ has been applied to the model Joule heating rate profiles. The respective height-integrated Joule heating rates are given in the legends.

and the associated height-integrated Joule heating rates for 12 bins. Figure 6 shows the q_J profiles binned with respect to the *Kp* index and MagLT.

As expected, the Joule heating rate increases with the *Kp* index which can be seen from the maxima of the vertical profiles and the height-integrated Joule heating rates given in Figure 6. This is found for both q_J^M and q_J^E. q_J^E is generally lowest in the noon MagLT sector and largest in the midnight MagLT sector. The important exception is for $Kp > 4$, where the largest q_J^E is actually found in the dusk MagLT sector. For the model runs, both driven by *Heelis* and *Weimer* convection, it is found that the Joule heating rate is lowest in the noon sector and largest in the midnight sector for all *Kp* ranges. The model profiles shown in Figure 6 have been scaled with the default factor $f = 1.5$. The *Heelis*-driven model Joule heating rates are generally lower than those constrained by EISCAT measurements for $Kp < 4$. This agrees with Figure 4 where it has been shown that *Heelis*-driven runs require a larger than default scaling factor at $Kp < 4$. At $Kp > 4$, however, q_J^M approximately fits the EISCAT-constrained q_J^E or even exceeds it for the noon sector, where q_J^E is overall lowest.

At $Kp < 4$, the default-scaled *Weimer*-driven TIE-GCM runs show Joule heating rates lower than q_J^E at all magnetic local times except for the midnight MagLT sector. For $Kp > 4$, however, the q_J^M profiles from *Weimer*-driven runs

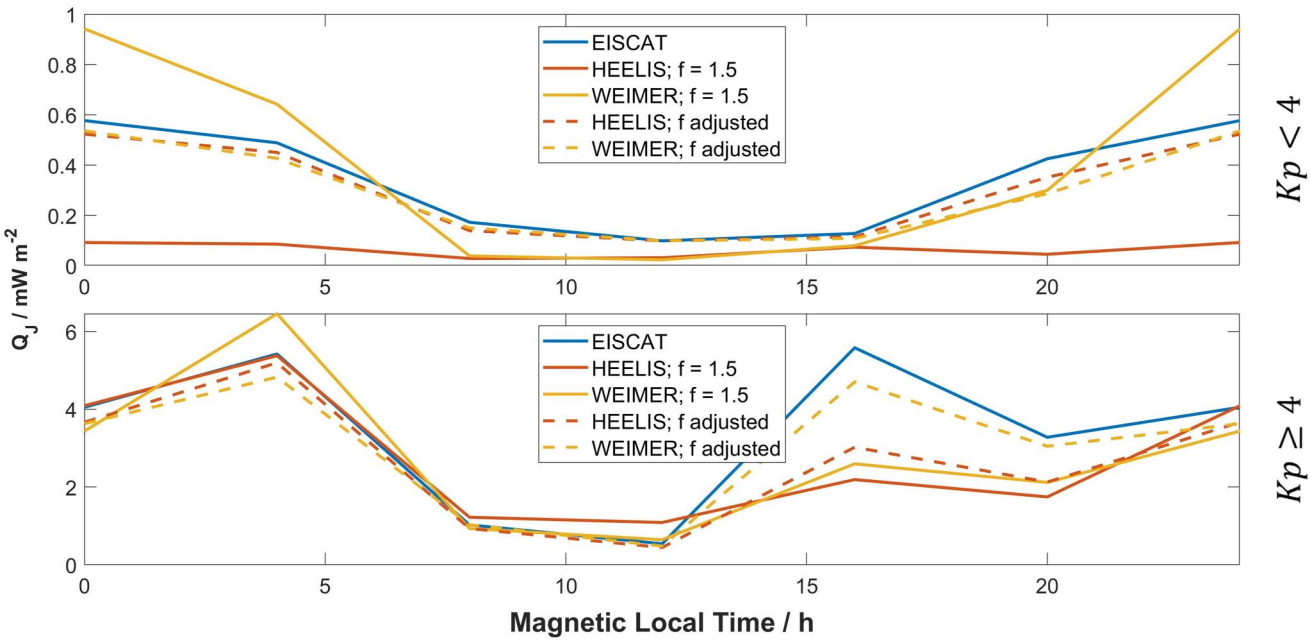

Figure 7. Variation of the height-integrated Joule heating rates Q_J^M and Q_J^E with magnetic local time for $Kp < 4$ (top) and $Kp \geq 4$ (bottom). The model results are shown as dashed lines for the default $f = 1.5$ and solid lines for an adjusted scaling factor.

fit the q_J^E profiles very well, except for the dusk MagLT sector. Here, the Joule heating is clearly underestimated by the model runs.

In summary, it can be seen from Figure 6 that the magnetic local time very much impacts the vertical Joule heating profiles q_J^M and q_J^E and the required scaling. This can also be seen from the variation of the height-integrated Joule heating rates Q_J^M and Q_J^E with magnetic local time shown in Figure 7. Two cases of geomagnetic activity, $Kp < 4$ and $Kp \geq 4$, are distinguished.

As noticed before, Figure 7 shows that Joule heating rates are largest during nighttime for $Kp < 4$. While the *Heelis*-driven runs give a very low height-integrated Joule heating rate at all MagLTs, Q_J^M from *Weimer*-driven runs is lower than Q_J^E during daytime and larger during nighttime. Adjusting the scaling factor would reduce the difference between EISCAT-constrained and model height-integrated Joule heating rates at all magnetic local times.

At $Kp > 4$, the Q_J^E maximum is around 16 MagLT, and the largest Q_J^M are found around 4 MagLT. It can be seen in Figure 6 that all model runs give distinctly larger Joule heating rates than the EISCAT-constrained calculations for $Kp > 4$, 3–9 MagLT. It should be noted that at $Kp > 4$, the *Heelis*-driven runs scaled with $f = 1.5$ reproduce Q_J^E extremely well at about 0–6 MagLT, while the *Weimer*-driven runs give Q_J^M very close to Q_J^E at around 6–12 MagLT. Therefore, the required scaling factor does not only change with the Kp index and convection model but also with magnetic local time. Similar to Figure 4a, the required scaling factors for the dawn, noon, dusk, and midnight MagLT sectors are shown in Figure 8.

The large scaling factor required for *Heelis*-driven runs at low Kp values seen in Figure 4 is mostly caused by the dawn and midnight sectors (see Figures 8a and 8d). During the noon and dusk sector in Figures 8b and 8c, the *Heelis*-driven runs underestimate the Joule heating for low Kp values less strongly. At high Kp values, the differences between Q_J^M and Q_J^E seems to be well accounted for by the default $f = 1.5$ except for the noon sector where f should be reduced.

The *Weimer*-driven TIE-GCM runs seem to underestimate the Joule heating rate at low Kp values during the dawn and noon sectors. During the dusk and midnight sectors, $f = 1.5$ seems to be appropriate in order to reproduce Q_J^E. In Figure 4, it has been noted that *Weimer*-driven model runs tend to underestimate the Joule heating rate more

10.1029/2023EA003447

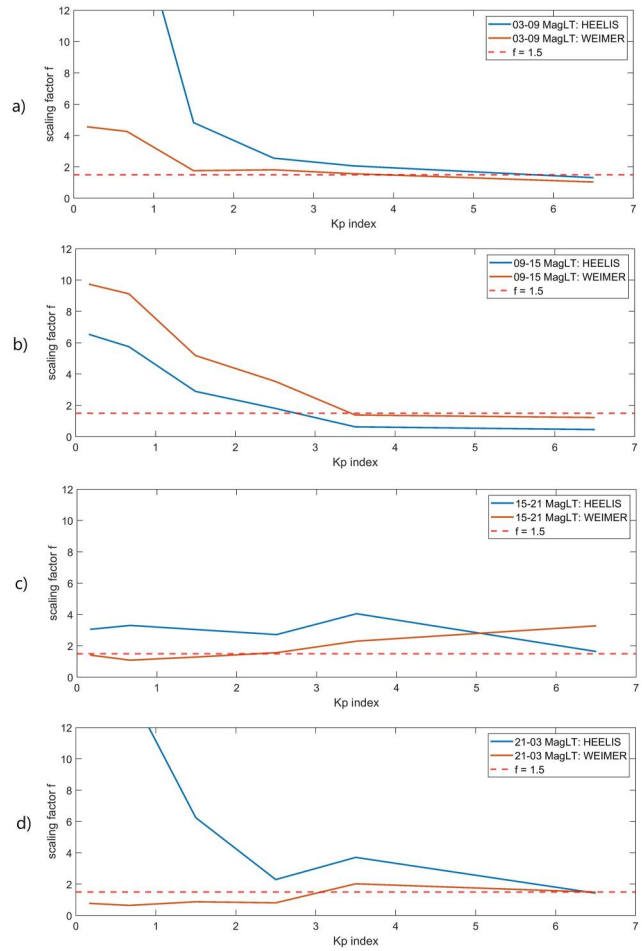

Figure 8. *Kp* index dependence of the required Joule heating scaling factor *f* for the different magnetic local time sectors (a) 03–09, (b) 09–15, (c) 15–21, and (d) 21–03.

than covered by $f = 1.5$ for $Kp > 4$. As can be seen in Figure 8c, this is actually only the case for the dusk MagLT sector where EISCAT-constrained Joule heating rates were largest. During all other MagLT sectors, $f = 1.5$ appears to be very close to the required scaling factor at $Kp > 4$.

In summary, the required scaling factor changes significantly not only with the *Kp* index but also with the magnetic local time. Adjusting the scaling factor f with respect to MagLT might therefore result in a notably better agreement of Joule heating rates calculated from measurement and model results. The E_{KL} dependence for different MagLT sectors is investigated with the bins listed in Table 3. The Joule heating profiles for the respective bins are shown in Figure 9, the model run profiles have again been scaled with $f = 1.5$.

It can be seen that the Joule heating rate generally but not strictly increases with E_{KL}. The strongest Joule heating is found for the midnight MagLT sector and the weakest Joule heating for the noon MagLT sector at all E_{KL} conditions. The MagLT dependence of the Joule heating rate therefore agrees well with Figure 6.

The *Heelis*-driven TIE-GCM runs give too low Joule heating rates in all 12 bins, indicating that in these runs E_{KL} and the Joule heating rate are not well correlated. This can be explained by the fact that *Heelis*-driven runs do not apply any solar wind information as input. However, the *Weimer*-driven runs show a behavior very similar to what has been found in Figure 6. At $E_{KL} > 0.5$ mVm^{-1} and in the MagLT midnight sector, *Weimer*-driven TIE-GCM runs give Joule heating profiles that fit q_J^E very well or even exceed them. At all other conditions, the model runs tend to underestimate the Joule heating. Figure 10 displays the variation of the height-integrated Joule heating rate with MagLT, distinguished for the two cases $E_{KL} < 0.5$ mVm^{-1} and $E_{KL} \geq 0.5$ mVm^{-1}.

10.1029/2023EA003447

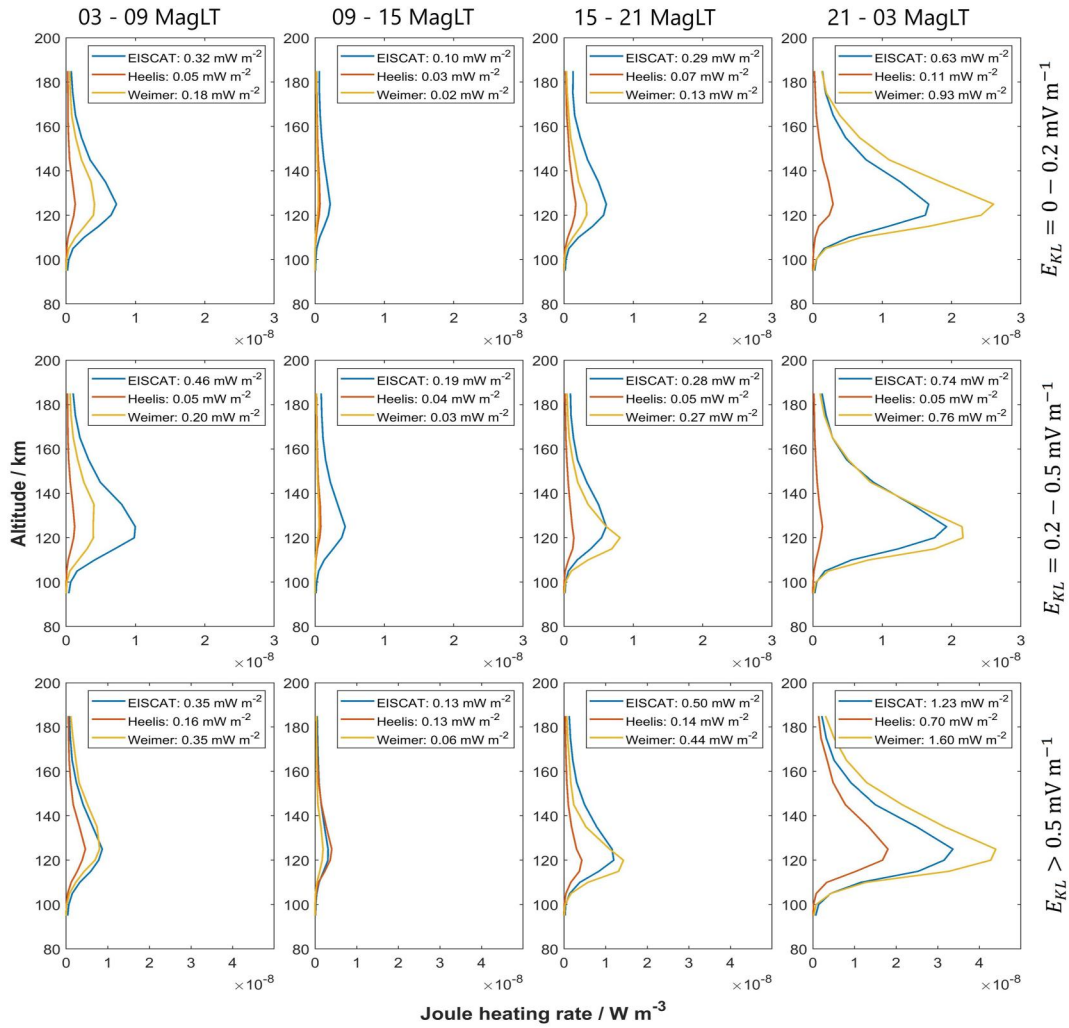

Figure 9. Median vertical profiles of the Joule heating rates q_J^M and q_J^E for 12 bins of varying E_{KL} and magnetic local time. The default $f = 1.5$ has been applied to the model Joule heating rate profiles. The respective height-integrated Joule heating rates are given in the legends.

For $E_{KL} < 0.5$ mVm^{-1}, the results are nearly equivalent to the $Kp < 4$ case shown in Figure 7. Q_J is generally largest at MagLT midnight and *Heelis*-driven runs give extremely low Joule heating rates at all magnetic local time sectors. The *Weimer*-driven runs overestimate the heating rate at nighttime and underestimate it at daytime. Adjusting the scaling factor would significantly decrease the difference between Q_J^M and Q_J^E for all magnetic local times.

For $E_{KL} \geq 0.5$ mVm^{-1}, the results are quite similar to the low geophysical activity conditions. The height-integrated Joule heating rate is largest during the midnight MagLT sector. The *Heelis*-driven TIE-GCM runs reproduce Q_J^E well at about 8–16 MagLT but strongly underestimate the Joule heating for all other times. The *Weimer*-driven runs also reproduce Q_J^E very well at about 8–16 MagLT and slightly overestimate it at most other magnetic local times. An adjustment of the scaling factor would improve the height-integrated Joule heating rate in both *Heelis*- and *Weimer*-driven runs at all magnetic local times compared to the EISCAT-constrained Joule heating rates.

For the four MagLT sectors investigated in Figure 9, the required scaling factors at different E_{KL} conditions are shown in Figure 11.

The distinctly larger Joule heating scaling required for *Heelis*-driven model runs at low E_{KL} values is mostly rooted in the dawn and midnight MagLT sectors shown in Figures 11a and 11d. This is similar to what has been

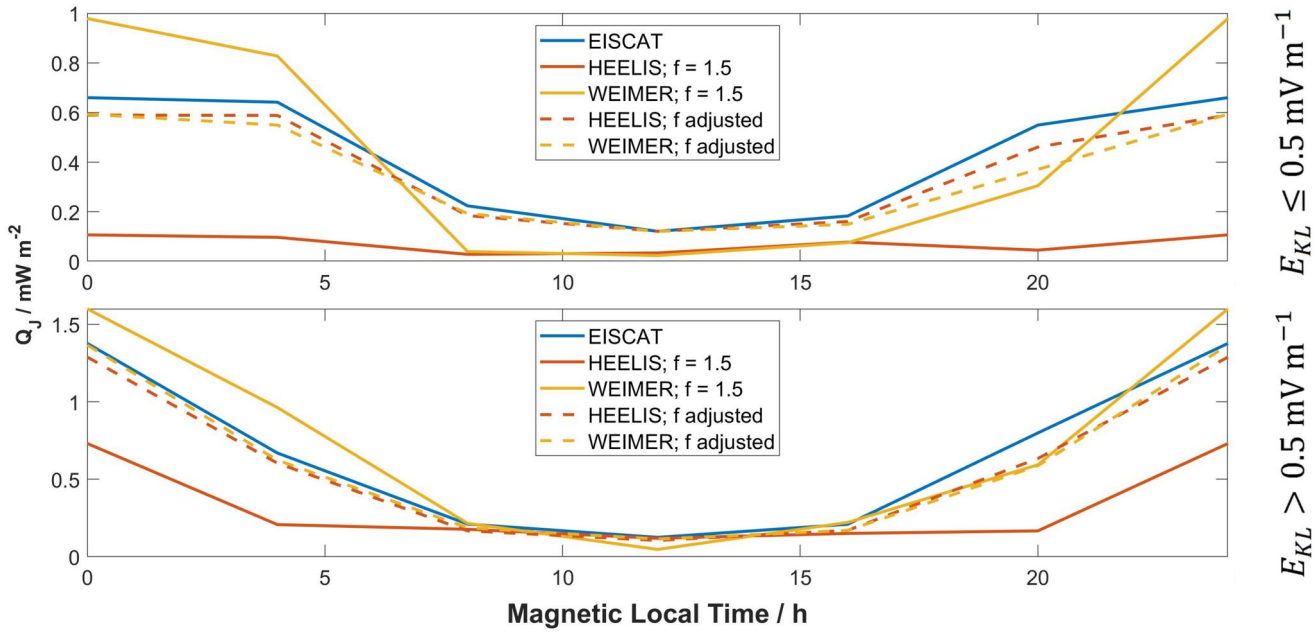

Figure 10. Variation of the height-integrated Joule heating rates Q_J^M and Q_J^E with magnetic local time for $E_{KL} < 0.5$ mVm^{-1} (top) and $E_{KL} \geq 0.5$ mVm^{-1} (bottom). The model results are shown as dashed lines for the default $f = 1.5$ and solid lines for an adjusted scaling factor.

found in Figure 8. However, as has been noted in Figure 9, the default $f = 1.5$ is too low for *Heelis*-driven runs under most E_{KL} and MagLT conditions. The exception is for $E_{KL} \gtrsim 0.8$ mVm^{-1} during the MagLT noon sector in Figure 11 where a scaling factor slightly lower than $f = 1.5$ would lead to the best fit. This is equivalent to what has been found for $Kp > 3$ in Figure 8.

For the *Weimer*-driven runs, the required scaling factor is very close to the default $f = 1.5$ for the majority of E_{KL} conditions and magnetic local times. The clearest deviation is found for $E_{KL} \lesssim 0.6$ mVm^{-1} during the noon MagLT sector though the required scaling factor is larger than 1.5 for all E_{KL} conditions in that sector. This agrees very well with Figures 7 and 8b, and 10 which all showed that the Joule heating rate is underestimated around MagLT noon time in *Weimer*-driven TIE-GCM runs.

The optimum scaling factors f_H and f_W for *Heelis*- and *Weimer*-driven TIE-GCM runs for 13 Kp bins and 9 E_{KL} bins are shown in Table 4. Tables 5 and 6 give the optimum scaling factors f_H and f_W for the four investigated MagLT sectors in three bins of Kp index and E_{KL} respectively.

5. Discussion

Codrescu et al. (1995) showed that a scaling of the Joule heating in global circulation models is necessary to account for the contribution of processes on time-scales not resolved in the models. The factor $f = 1.5$ has been implemented in the TIE-GCM as the default factor and, as shown in this study, seems to be appropriate as average factor for all convection models, magnetic local times and geophysical conditions. The general trend that the largest q_J occurs around midnight and the lowest q_J is observed around noon magnetic local time agrees well with previous studies (e.g., Baloukidis et al., 2023; Rodger et al., 2001). The exception is that when applying EISCAT plasma parameters at $Kp > 4$, the strongest Joule heating is found in the dusk MagLT sector. Foster et al. (1983) reported a maximum of Joule heating rates in the MagLT dusk sector for $3 \leq Kp \leq 6$ during summer. However, since our data includes comparably few measurements during summer, the dusk maximum of Joule heating found in this paper might not be related to the findings by Foster et al. (1983). Baloukidis et al. (2023) showed that this trend is also found in TIE-GCM runs driven by the *Weimer* convection model. However, the variation of Joule heating with magnetic local time is not exactly reproduced by the model which introduces increased heating rates for MagLT noon time and lower heating rates during the rest of the day (Baloukidis et al., 2023). Similarly, they showed an increase of the Joule heating rate with increasing Kp index, though the trend is not equally strong in Joule heating rates calculated from measurements and model results. The findings of Baloukidis et al. (2023)

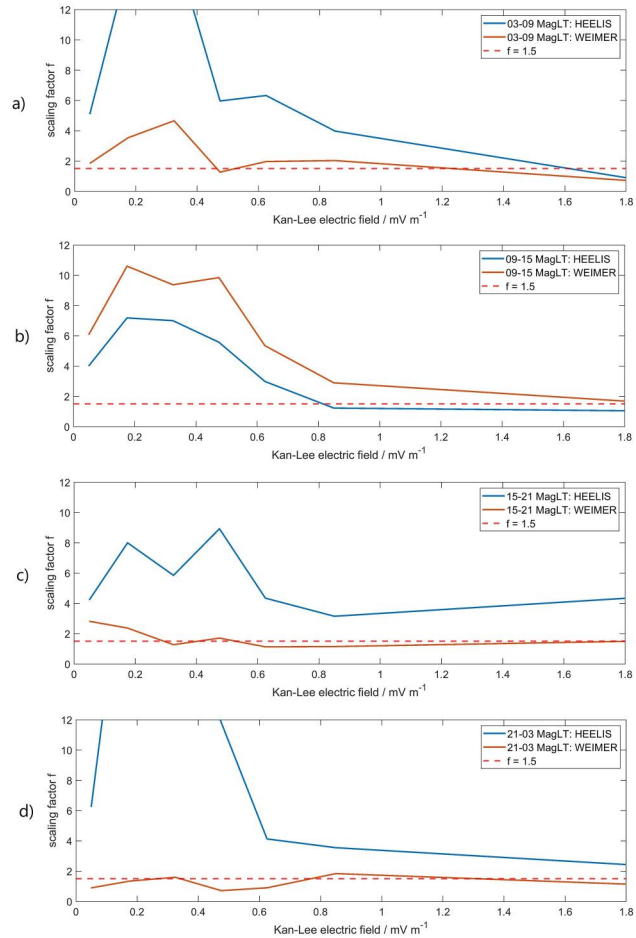

Figure 11. E_{KL} dependence of the required Joule heating scaling factor f for the different magnetic local time sectors (a) 03–09, (b) 09–15, (c) 15–21, and (d) 21–03.

Table 4
Adjusted Scaling Factors f_H and f_W for Heelis- and Weimer-Driven Model Runs With Respect to Kp Index and E_{KL}

Kp	f_H	f_W	E_{KL} (mVm^{-1})	f_H	f_W
0	9.50	3.97	**0–0.1**	4.76	2.09
0.333	8.49	2.53	**0.1–0.2**	10.44	2.72
0.667	10.26	2.00	**0.2–0.35**	12.11	4.21
1	4.96	2.19	**0.35–0.5**	8.44	1.82
1.333	5.00	1.84	**0.5–0.7**	5.44	1.45
1.667	3.53	2.14	**0.7–0.9**	3.35	1.44
2	3.05	1.78	**0.9–1.15**	1.40	1.21
2.333–2.667	2.16	1.91	**1.15–1.6**	2.19	0.93
3–3.333	2.63	1.46	**>1.6**	1.38	0.67
3.667–4	1.77	1.59			
4.333–5	1.59	1.61			
5.333–6	1.24	1.60			
>6	0.77	2.89			

Table 5
Adjusted Scaling Factor f_H and f_W for Heelis- and Weimer-Driven Model Runs With Respect to the Kp Index and MagLT

Kp/MagLT	03–09	09–15	15–21	21–03
0–2	$f_H = 13.32$	$f_H = 5.59$	$f_H = 3.45$	$f_H = 18.91$
	$f_W = 3.16$	$f_W = 8.31$	$f_W = 1.40$	$f_W = 0.87$
2–4	$f_H = 2.68$	$f_H = 1.32$	$f_H = 3.57$	$f_H = 2.89$
	$f_W = 1.88$	$f_W = 2.90$	$f_W = 2.20$	$f_W = 1.24$
4–9	$f_H = 1.31$	$f_H = 0.46$	$f_H = 1.64$	$f_H = 1.43$
	$f_W = 1.04$	$f_W = 1.23$	$f_W = 3.28$	$f_W = 1.49$

could be mostly confirmed in this paper and extended by also considering *Heelis*-driven TIE-GCM runs as well as variations with the Kan-Lee merging electric field E_{KL}.

Past studies have shown that it is advantageous to adjust the scaling factor with regard to certain parameters, for example, in Emery et al. (1999) $f = 1.5$ was applied in the winter and $f = 2.5$ in the summer hemisphere. Foster et al. (1983) showed a strong seasonal dependence of the height-integrated Joule heating rate. It is likely that this variation, similar to the variation with geophysical activity and MagLT, is not exactly reproduced by the models. However, as shown in Figure 1, the measurements investigated in this paper are not equally spread across the year and, thus, a detailed analysis of the scaling parameter for all seasons with similar statistics is not yet feasible from the available database.

It should be considered, that not only the models but also the measurements do not resolve all processes contributing to the spatial and temporal variations of Joule heating. Codrescu et al. (1995) noted that there is a considerable variability of the electric field on time-scales $\lesssim$5 min that leads to an underestimation of Joule heating rates. The measurement resolution of 6 min applied in this paper, therefore, does not include the contribution of fast-dynamic processes either. Brekke and Kamide (1996) showed that frictional heating terms related to the inertia of the ions lead to a heating contribution of oscillating electric fields. Fast-changing electric fields on a time-scale $\sim$1 s could increase the maximum of the Joule heating rate profile by about 10% (Brekke & Kamide, 1996). However, these time-scales are currently far below the resolution of both ISR measurements and T-I models. But it can be assumed that the required scaling of model Joule heating rates has to be further adjusted once measurements are able to resolve shorter time-scales.

One major assumption for the present study was the application of TIE-GCM neutral winds and ion-neutral collision frequencies for both measurement and model calculations. It is possible to calculate neutral winds from EISCAT CP2 measurements (Brekke et al., 1973; Günzkofer et al., 2022; Nozawa et al., 2010) but this, in turn, requires knowledge of the ion-neutral collision frequency. The ion-neutral collision frequency can be measured from dual-frequency EISCAT experiments (Grassmann, 1993; Günzkofer, Liu, et al., 2023; Günzkofer, Stober, et al., 2023; Nicolls et al., 2014) which is not possible in combination with beam-swing measurements. A direct measurement of the collision frequency, and subsequently the neutral wind, would lead to more accurate Joule heating rate estimations and allow for a better evaluation of the model results.

Table 6
Adjusted Scaling Factor f_H and f_W for Heelis- and Weimer-Driven Model Runs With Respect to E_{KL} and MagLT

E_{KL} (mVm^{-1})/MagLT	03–09	09–15	15–21	21–03
0–0.2	$f_H = 8.90$	$f_H = 4.49$	$f_H = 5.61$	$f_H = 9.27$
	$f_W = 2.52$	$f_W = 6.62$	$f_W = 2.86$	$f_W = 1.00$
0.2–0.5	$f_H = 13.00$	$f_H = 7.62$	$f_H = 6.25$	$f_H = 21.15$
	$f_W = 3.42$	$f_W = 10.63$	$f_W = 1.18$	$f_W = 1.27$
>0.5	$f_H = 3.04$	$f_H = 1.28$	$f_H = 4.47$	$f_H = 2.92$
	$f_W = 1.51$	$f_W = 2.61$	$f_W = 1.30$	$f_W = 1.14$

It should also be noted that the energy deposition by Joule heating strongly depends on the local position within the convection pattern (Foster et al., 1983). So in addition to the strength of the convection pattern, that is, the electric fields and the ion velocities, the size and shape of the convection pattern are of high importance. Both, the *Heelis* and the *Weimer* convection model, have been shown to struggle with giving the accurate size of the convection pattern (Pokhotelov et al., 2008). One possible improvement might be the application of the *assimilative mapping of ionospheric electrodynamics* method to obtain the high-latitude plasma convection (Cousins et al., 2013; Pokhotelov et al., 2021; Richmond & Kamide, 1988).

6. Conclusion

It has been shown that Joule heating rates calculated from EISCAT plasma and TIE-GCM neutral parameters vary similarly with respect to the *Kp* index, the Kan-Lee merging electric field E_{KL} and the magnetic local time as Joule heating rates calculated from only TIE-GCM parameters. However, the variations are not equally strong and, therefore, the empirical scaling of Joule heating rates in TIE-GCM runs should be adjusted with respect to these parameters. Significant differences between TIE-GCM runs driven with the *Heelis* and *Weimer* convection models have been found and the scaling factor should be adjusted with respect to this as well. The measurement-constrained Joule heating rate changes drastically with magnetic local time with the largest heating rates in the midnight sector (for $Kp < 4$ and all E_{KL} values) and the dusk sector (for $Kp > 4$). While the model runs generally show the same trend, it can be seen that the required scaling factor is distinctly different for the investigated MagLT sectors. In conclusion, it has been shown that the choice of polar plasma convection model, the magnetic local time, and the geophysical conditions, that is, the *Kp* index and the Kan-Lee merging electric field, impact the required scaling factor. The seasonal dependence of the required scaling factor cannot be determined with the current measurement data set. Applying the adjusted scaling factor f found in our study would bring the Joule heating rate estimation by the TIE-GCM closer to the Joule heating rates calculated from EISCAT plasma parameters.

For future investigations, extending the data set to sufficiently cover all seasons is crucial. The current gaps in the data set are due to the fact that only certain measurements with the EISCAT ISR, that is, *CP2* campaigns, can be applied to derive Joule heating rates. The upcoming EISCAT_3D system (McCrea et al., 2015) will be a major advance as the phased-array concept allows for multi-beam measurements and therefore does not require the rotation of a large radar dish. The EISCAT_3D radar will allow to create a large database suitable for the derivation of Joule heating rates within a short time of operation. Another advantage of phased-array multi-beam experiments is the possibility to perform pulse-to-pulse beam steering or software beam forming to collect data from many different beam directions without the need to mechanically steer the beam. Since all radar beams are available at nearly the same time, the time resolution of 3D ion velocity vectors will be the same as for the other ISR plasma parameters.

Acknowledgments
EISCAT is an international association supported by research organizations in China (CRIRP), Finland (SA), Japan (NIPR and ISEE), Norway (NFR), Sweden (VR), and the United Kingdom (UKRI). The TIE-GCM and related Thermosphere-Ionosphere models have been developed by the "Atmosphere Ionosphere Magnetosphere" (AIM) Section of the High Altitude Observatory (HAO) at NCAR (see http://www.hao.ucar.edu/modeling/tgcm). The TIE-GCM data was generated on the "Kratos" High-Performance Data Analysis Cluster (HPDA) at the German Aerospace Center (DLR) Jena. Gunter Stober is a member of the Oeschger Center for Climate Change Research (OCCR). Huixin Liu acknowledges supports by JSPS Grants 17KK0095, 18H01270, 20H00197, 22K21345. This work is carried out at Kyushu University with the support of the SCOSTEP SVS program and the JSPS PBASE program. Open Access funding enabled and organized by Projekt DEAL.

Data Availability Statement

The data are available under the Creative Commons Attribution 4.0 International license at https://doi.org/10.5281/zenodo.10162944 (Günzkofer, Liu, et al., 2023).

References

Alken, P., Thébault, E., Beggan, C. D., Amit, H., Aubert, J., Baerenzung, J., et al. (2021). International geomagnetic reference field: The thirteenth generation. *Earth Planets and Space*, *73*(1), 49. https://doi.org/10.1186/s40623-020-01288-x

Baloukidis, D., Sarris, T., Tourgaidis, S., Pirnaris, P., Aikio, A., Virtanen, I., et al. (2023). A comparative assessment of the distribution of Joule heating in altitude as estimated in TIE-GCM and EISCAT over one solar cycle. *Journal of Geophysical Research: Space Physics*, *128*(12), e2023JA031526. https://doi.org/10.1029/2023JA031526

Barraclough, D. R. (1988). IAGA division I working group 1: International geomagnetic reference field revision 1987. *Geophysical Journal International*, *93*(1), 187–189. https://doi.org/10.1111/j.1365-246X.1988.tb01397.x

Baumjohann, W., & Treumann, R. A. (1996). *Basic space plasma physics*. Imperial College Press. https://doi.org/10.1142/p015

Brekke, A., Doupnik, J. R., & Banks, P. M. (1973). A preliminary study of the neutral wind in the auroral E region. *Journal of Geophysical Research*, *78*(34), 8235–8250. https://doi.org/10.1029/JA078i034p08235

Brekke, A., & Kamide, Y. (1996). On the relationship between Joule and frictional heating in the polar ionosphere. *Journal of Atmospheric and Terrestrial Physics*, *58*(1), 139–143. https://doi.org/10.1016/0021-9169(95)00025-9

Codrescu, M. V., Fuller-Rowell, T. J., & Foster, J. C. (1995). On the importance of E-field variability for Joule heating in the high-latitude thermosphere. *Geophysical Research Letters*, *22*(17), 2393–2396. https://doi.org/10.1029/95GL01909

Cousins, E. D. P., Matsuo, T., & Richmond, A. D. (2013). SuperDARN assimilative mapping. *Journal of Geophysical Research: Space Physics*, *118*(12), 7954–7962. https://doi.org/10.1002/2013JA019321

Deng, Y., Maute, A., Richmond, A. D., & Roble, R. G. (2009). Impact of electric field variability on Joule heating and thermospheric temperature and density. *Geophysical Research Letters*, *36*(8), L08105. https://doi.org/10.1029/2008GL036916

Deng, Y., & Ridley, A. J. (2007). Possible reasons for underestimating Joule heating in global models: E field variability, spatial resolution, and vertical velocity. *Journal of Geophysical Research*, *112*(A9), A09308. https://doi.org/10.1029/2006JA012006

Emery, B. A., Lathuillere, C., Richards, P. G., Roble, R. G., Buonsanto, M. J., Knipp, D. J., et al. (1999). Time dependent thermospheric neutral response to the 2-11 November 1993 storm period. *Journal of Atmospheric and Solar-Terrestrial Physics*, *61*(3–4), 329–350. https://doi.org/10.1016/S1364-6826(98)00137-0

Folkestad, K., Hagfors, T., & Westerlund, S. (1983). EISCAT: An updated description of technical characteristics and operational capabilities. *Radio Science*, *18*(6), 867–879. https://doi.org/10.1029/RS018i006p00867

Foster, J. C., St. -Maurice, J. P., & Abreu, V. J. (1983). Joule heating at high latitudes. *Journal of Geophysical Research*, *88*(A6), 4885–4897. https://doi.org/10.1029/JA088iA06p04885

Grassmann, V. (1993). An incoherent scatter experiment for the measurement of particle collisions. *Journal of Atmospheric and Terrestrial Physics*, *55*(4–5), 573–576. https://doi.org/10.1016/0021-9169(93)90006-K

Günzkofer, F., Liu, H., Stober, G., Pokhotelov, D., & Borries, C. (2023). Evaluation of the empirical scaling factor of Joule heating rates in TIE-GCM with EISCAT measurements [Dataset]. *Zenodo*. https://doi.org/10.5281/zenodo.10162944

Günzkofer, F., Pokhotelov, D., Stober, G., Liu, H., Liu, H. L., Mitchell, N. J., et al. (2022). Determining the origin of tidal oscillations in the ionospheric transition region with EISCAT radar and global simulation data. *Journal of Geophysical Research: Space Physics*, *127*(10), e2022JA030861. https://doi.org/10.1029/2022JA030861

Günzkofer, F., Stober, G., Pokhotelov, D., Miyoshi, Y., & Borries, C. (2023). Difference spectrum fitting of the ion-neutral collision frequency from dual-frequency EISCAT measurements. *Atmospheric Measurement Techniques*, *16*(23), 5897–5907. https://doi.org/10.5194/amt-16-5897-2023

Hagan, M. E., & Forbes, J. M. (2002). Migrating and nonmigrating diurnal tides in the middle and upper atmosphere excited by tropospheric latent heat release. *Journal of Geophysical Research*, *107*(D24), 4754. https://doi.org/10.1029/2001JD001236

Hagan, M. E., & Forbes, J. M. (2003). Migrating and nonmigrating semidiurnal tides in the upper atmosphere excited by tropospheric latent heat release. *Journal of Geophysical Research*, *108*(A2), 1062. https://doi.org/10.1029/2002JA009466

Heelis, R. A., Lowell, J. K., & Spiro, R. W. (1982). A model of the high-latitude ionospheric convection pattern. *Journal of Geophysical Research*, *87*(A8), 6339–6345. https://doi.org/10.1029/JA087iA08p06339

Huang, Y., Richmond, A. D., Deng, Y., & Roble, R. (2012). Height distribution of Joule heating and its influence on the thermosphere. *Journal of Geophysical Research*, *117*(A8), A08334. https://doi.org/10.1029/2012JA017885

Kan, J. R., & Lee, L. C. (1979). Energy coupling function and solar wind-magnetosphere dynamo. *Geophysical Research Letters*, *6*(7), 577–580. https://doi.org/10.1029/GL006i007p00577

Kavanagh, A. J., Ogawa, Y., & Woodfield, E. E. (2022). Two techniques for determining F-region ion velocities at meso-scales: Differences and impacts on Joule heating. *Journal of Geophysical Research: Space Physics*, *127*(6), e30062. https://doi.org/10.1029/2021JA030062

Kelley, M. C. (2009). *The Earth's ionosphere: Plasma physics and electrodynamics* (2nd ed.). Elsevier Academic Press.

Laundal, K. M., & Richmond, A. D. (2017). Magnetic coordinate systems. *Space Science Reviews*, *206*(1–4), 27–59. https://doi.org/10.1007/s11214-016-0275-y

Maute, A. (2017). Thermosphere-ionosphere-electrodynamics general circulation model for the ionospheric connection explorer: TIEGCM-ICON. *Space Science Reviews*, *212*(1–2), 523–551. https://doi.org/10.1007/s11214-017-0330-3

McCrea, I., Aikio, A., Alfonsi, L., Belova, E., Buchert, S., Clilverd, M., et al. (2015). The science case for the EISCAT_3D radar. *Progress in Earth and Planetary Science*, *2*(1), 21. https://doi.org/10.1186/s40645-015-0051-8

Nicolls, M. J., Bahcivan, H., Häggström, I., & Rietveld, M. (2014). Direct measurement of lower thermospheric neutral density using multi-frequency incoherent scattering. *Geophysical Research Letters*, *41*(23), 8147–8154. https://doi.org/10.1002/2014GL062204

Nozawa, S., Ogawa, Y., Oyama, S., Fujiwara, H., Tsuda, T., Brekke, A., et al. (2010). Tidal waves in the polar lower thermosphere observed using the EISCAT long run data set obtained in September 2005. *Journal of Geophysical Research*, *115*(A8), A08312. https://doi.org/10.1029/2009JA015237

Nygrén, T., Aikio, A. T., Kuula, R., & Voiculescu, M. (2011). Electric fields and neutral winds from monostatic incoherent scatter measurements by means of stochastic inversion. *Journal of Geophysical Research*, *116*(A5), A05305. https://doi.org/10.1029/2010JA016347

Palmroth, M., Janhunen, P., Pulkkinen, T. I., Aksnes, A., Lu, G., Østgaard, N., et al. (2005). Assessment of ionospheric Joule heating by GUMICS-4 MHD simulation, AMIE, and satellite-based statistics: Towards a synthesis. *Annales Geophysicae*, *23*(6), 2051–2068. https://doi.org/10.5194/angeo-23-2051-2005

Pokhotelov, D., Fernandez-Gomez, I., & Borries, C. (2021). Polar tongue of ionisation during geomagnetic superstorm. *Annales Geophysicae*, *39*(5), 833–847. https://doi.org/10.5194/angeo-39-833-2021

Pokhotelov, D., Mitchell, C. N., Spencer, P. S. J., Hairston, M. R., & Heelis, R. A. (2008). Ionospheric storm time dynamics as seen by GPS tomography and in situ spacecraft observations. *Journal of Geophysical Research*, *113*(A3), A00A16. https://doi.org/10.1029/2008JA013109

Rich, F. J., Gussenhoven, M. S., Hardy, D. A., & Holeman, E. (1991). Average height-integrated Joule heating rates and magnetic deflection vectors due to field-aligned currents during sunspot minimum. *Journal of Atmospheric and Terrestrial Physics*, *53*(3–4), 293–308. https://doi.org/10.1016/0021-9169(91)90113-L

Richmond, A. D., & Kamide, Y. (1988). Mapping electrodynamic features of the high-latitude ionosphere from localized observations. *Technique*, *93*(A6), 5741–5759. https://doi.org/10.1029/JA093iA06p05741

Richmond, A. D., Ridley, E. C., & Roble, R. G. (1992). A thermosphere/ionosphere general circulation model with coupled electrodynamics. *Geophysical Research Letters*, *19*(6), 601–604. https://doi.org/10.1029/92GL00401

Rodger, A. S., Wells, G. D., Moffett, R. J., & Bailey, G. J. (2001). The variability of Joule heating, and its effects on the ionosphere and thermosphere. *Annales Geophysicae*, *19*(7), 773–781. https://doi.org/10.5194/angeo-19-773-2001

Schunk, R., & Nagy, A. (2009). *Ionospheres: Physics, plasma physics, and chemistry*. Cambridge Academic Press. https://doi.org/10.1017/CBO9780511635342

Thayer, J. P. (1998). Height-resolved Joule heating rates in the high-latitude E region and the influence of neutral winds. *Journal of Geophysical Research*, *103*(A1), 471–487. https://doi.org/10.1029/97JA02536

Thayer, J. P. (2000). High-latitude currents and their energy exchange with the ionosphere-thermosphere system. *Journal of Geophysical Research*, *105*(A10), 23015–23024. https://doi.org/10.1029/1999JA000409

Tjulin, A. (2021). *Eiscat experiments* (Technical Report). EISCAT Scientific Association. Retrieved from https://eiscat.se/wp-content/uploads/2021/03/Experiments_v20210302.pdf

Vickrey, J. F., Vondrak, R. R., & Matthews, S. J. (1982). Energy deposition by precipitating particles and Joule dissipation in the auroral ionosphere. *Journal of Geophysical Research*, *87*(A7), 5184–5196. https://doi.org/10.1029/JA087iA07p05184

Weimer, D. R. (1995). Models of high-latitude electric potentials derived with a least error fit of spherical harmonic coefficients. *Journal of Geophysical Research*, *100*(A10), 19595–19608. https://doi.org/10.1029/95JA01755

Weimer, D. R. (2005). Improved ionospheric electrodynamic models and application to calculating Joule heating rates. *Journal of Geophysical Research*, *110*(A5), A05306. https://doi.org/10.1029/2004JA010884